

Measurement and modeling of electron-cloud-induced betatron tune shifts at CESR-TA

S. Poprocki,* S.W. Buechele, J.A. Crittenden, K. Rowan, D.L. Rubin, and J.E. San Soucie
CLASSE, Cornell University, Ithaca, NY 14853, USA

(Dated: May 11, 2022)

We report on extensive measurements at the Cornell Electron-positron Storage Ring of electron-cloud-induced betatron tune shifts for trains of positron bunches at 2.1 and 5.3 GeV with bunch populations ranging between 0.4×10^{10} and 9.5×10^{10} . Measurements using a witness bunch with variable distance from the end of the train and variable bunch population inform the study of cloud decay and cloud pinching during the bunch passage. We employ Monte Carlo simulations of the reflection and absorption of synchrotron radiation photons to determine the pattern of absorption sites around the circumference of the storage ring. The Geant4 simulation toolkit is used to model the interactions of the photons with the beampipe wall and determine the production energy and location distributions of the photoelectrons which seed the electron cloud. An electron cloud buildup model based on these distributions successfully describes the tune shift measurements after determining ring-averaged secondary-yield properties of the vacuum chamber using an iterative parameter optimization procedure.

I. INTRODUCTION

The buildup of low-energy electron densities in the vacuum chamber of a positron storage ring can result in betatron tune shifts, instabilities and emittance growth. We describe techniques to measure distortion of beam optics due to electron cloud (EC), application of these techniques to measure tune shifts and the development of predictive models of electron cloud phenomena.

The Cornell Electron-positron Storage Ring (CESR) was re-configured as a test accelerator in 2008 [1]. A comprehensive summary of the project, which included electron-cloud buildup and low-emittance lattice studies, can be found in the CESR-TA Phase I Report [2]. The results reported here concern three lattice configurations of the CESR ring: the test accelerator configurations at 2.1 GeV and at 5.3 GeV, and the 6.0 GeV upgrade to be commissioned in 2019. Table I lists the parameters of these three lattice configurations.

In Sec. II below we discuss and compare methods of measuring bunch-by-bunch betatron tune shifts. A comprehensive set of measurements along trains of positron bunches at 2.1 GeV and 5.3 GeV is shown. We describe in Sec. III the full procedure of electron cloud simulation starting with the generation of photons from synchrotron radiation, tracking of the photons in a 3D model of the vacuum chamber including reflections and absorption of the photons, the production of photoelectrons, the buildup of electron densities along a train of bunches, and the calculation of betatron tune shifts.

Although electron cloud buildup models have been successful in simulating tune shifts [3, 4] and vertical emittance growth [5] in general agreement with measurements, their predictive power has been limited by ad hoc assumptions. Furthermore, no single set of parameters has yet reproduced in simulation measurements of horizontal and vertical tune shifts over as wide a range of

TABLE I. Lattice parameters for the three configurations of the CESR ring addressed in this report: the 2.1 GeV and 5.3 GeV lattice for which betatron tune shifts were measured and for which simulations were performed, and the 6.0 GeV configuration for which the model was used to assess effects of electron cloud buildup on performance.

Beam energy (GeV)	2.085	5.289	6.000
Circumference (m)	768.44		
Bunch current (mA)	0.4–0.7	2.0–6.0	2.2–4.4
Number of bunches	30	20	45–90
Beam current (mA)	12–21	40–120	200
RF frequency (MHz)	500		
Energy loss per turn (MeV)	0.19	1.1	1.8
Momentum compaction (10^{-3})	6.7	9.2	5.7
Bunch length (mm)	9.2	15.8	15.6
Energy spread (10^{-4})	8.1	6.5	7.6
Horizontal tune	14.5639	11.2853	16.545
Vertical tune	9.5984	8.7914	12.63
Synchrotron tune	0.07354	0.04623	0.03416
Horizontal emittance (nm)	3.2	97	30
Vertical emittance (nm)	0.035	1	0.1

bunch populations and beam energies as shown in this work.

In an effort to improve the predictive power of the model for tune shifts and emittance growth, we employ the Synrad3D [6] and Geant4 [7] codes to calculate azimuthal distributions of absorbed photons, quantum efficiencies, and photoelectron energy distributions around the vacuum chamber throughout the circumference of the CESR ring [8, 9]. Secondary electron yield (SEY) parameters are fit to the large data set of betatron tune shift measurements collected at CESR.

Section IV discusses these results and draws conclusions about how betatron tunes respond to various cloud buildup characteristics. Finally, the model with the best-fit secondary yield parameters is applied to obtain estimates for the consequences of electron cloud buildup for

* E-mail: stp44@cornell.edu

operation of the major CESR upgrade to be completed in 2018 [10].

II. TUNE SHIFT MEASUREMENT

Tune shifts have been measured in a number of ways at CESR-TA. The most straightforward technique is to kick the entire train at once with a single-turn pinger and then record turn-by-turn position data for each bunch. An FFT of the position data yields the betatron tune [2, 11]. However, multiple peaks from coupled-bunch motion contaminate the signal. In addition, only vertical tune shift measurements using vertical pinger kicks are reliable with this method. The development of a vertical band of electron cloud density in dipole magnets (see Sec. III), *i.e.* a strong horizontal asymmetry on the scale of the beam size, is an important contribution to the tune shifts. A horizontal ping kick moves the bunch train coherently, and thus the cloud as well, so the measured horizontal tune shifts are suppressed by this measurement technique, since the test bunch receives no coherent kick from a cloud symmetric about its position. Better results are obtained by enabling bunch-by-bunch feedback on the train, disabling it one bunch at a time and measuring the tune of that bunch. The self-excitation (no external kick applied) is enough to get a signal, but the precision is improved by kicking the single bunch with a gated strip-line kicker.

The technique is further refined by using a digital tune tracker (DTT) [12]. The DTT phase-locks a digital oscillator to an observed betatron signal, and thus provides a frequency source for coherent excitation of steady state betatron motion. It also provides a digital clock that is synchronized to the instantaneous betatron motion, which can be used for synchronous detection of betatron signals. Typically, both horizontal and vertical modes are phase-locked simultaneously. However, in the betatron tune shift measurements shown here, although feedback was disabled for a single bunch in both horizontal and vertical planes, the excitation and tune measurement with the DTT was done separately in horizontal and vertical planes for practical reasons. Since measuring the tune shift through the train one bunch at a time can take some time, bunch currents were monitored and topped off between measurements as needed—typically every 1-5 bunches.

Tune shifts using the pinging method for 20-bunch trains of positrons at 5.3 GeV for several values of the bunch current are shown in Fig. 1. The bunch spacing is 14 ns. The magnitude of the tune shifts can be compared to the revolution frequency of 390 kHz. Large bunch-to-bunch fluctuations as well as overlap of data are observed. The tune shift measurements obtained using the digital tune tracker are shown in Fig. 2, and exhibit vertical tune shifts increasing monotonically with bunch current. These measurements are more reliable than those obtained via the pinging method since the single bunch

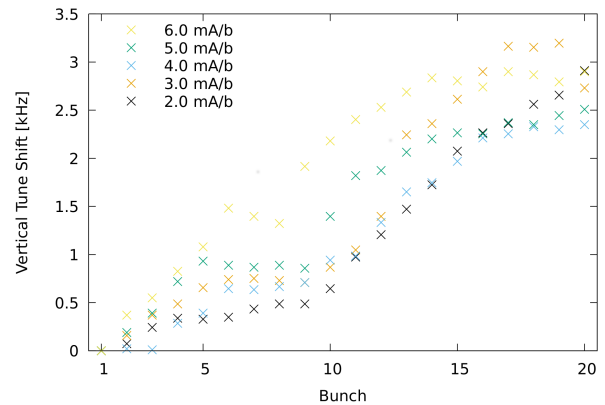


FIG. 1. Vertical betatron tune shifts measured using the “pinging” method along a 20-bunch train of positrons at 5.3 GeV for values of the bunch current ranging from 2 to 6 mA/b ($3.2\text{--}9.5 \times 10^{10}$ bunch populations).

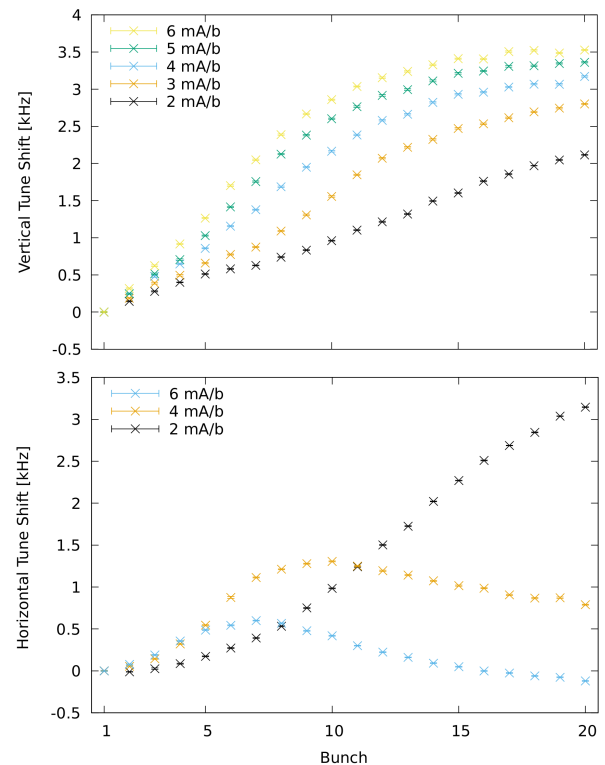


FIG. 2. Vertical (top) and horizontal (bottom) tune shifts measured using the digital tune tracker for a 20 bunch train of positrons with values for the bunch current ranging between 2 and 6 mA/b ($3.2\text{--}9.5 \times 10^{10}$ bunch populations) at 5.3 GeV. Data were recorded separately for each of the two planes.

tune measurement using the DTT is more accurate, and the rest of the train is stabilized via feedback.

The horizontal tune shift measurements exhibit a remarkable behavior where the tune shift along the train decreases for later bunches and higher currents. Our modeling shows this effect to result from the “cloud split-

ting” behavior in dipoles where the vertical stripe of cloud widens and splits into two stripes. This splitting is caused by cloud electron energies in the vertical mid-plane exceeding the peak energy of the SEY curve owing to the greater kicks from the higher bunch populations.

Tune shift measurements taken with the digital tune tracker for positrons at 2.1 GeV are shown in Fig. 3. The fluctuations observed in the vertical tune shift measurements at 0.7 mA/b were reduced in subsequent measurements at the other bunch currents by averaging over measurements at an increased acquisition rate. The hori-

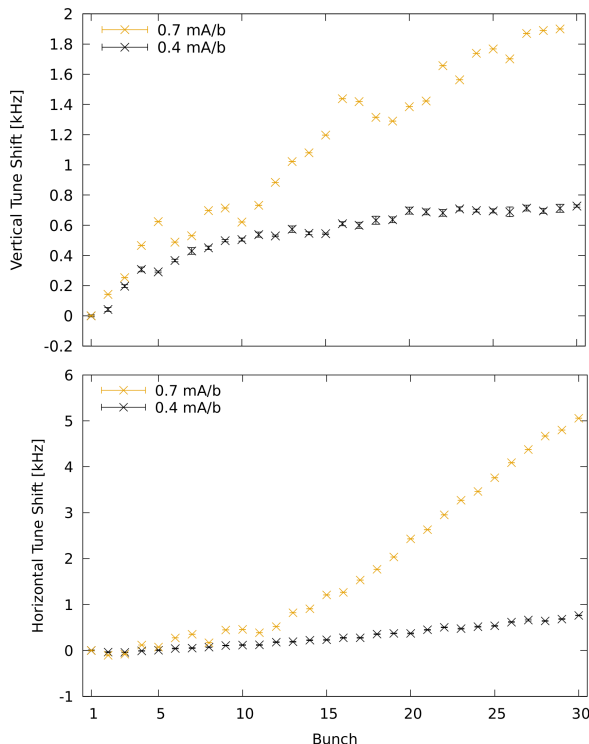


FIG. 3. Vertical (top) and horizontal (bottom) tune shifts measured using the digital tune tracker for a 30 bunch train of positrons at 0.4 and 0.7 mA/b (0.64×10^{10} and 1.12×10^{10} bunch populations) at 2.1 GeV.

zontal tune shift shows a great sensitivity to the bunch current, increasing by more than a factor of 5 as the bunch current increases from 0.4 to 0.7 mA/b. This threshold-type behavior was accompanied by a sharp increase in vertical beam size along the train, as described in Ref. [13]. The linear increase with bunch number beginning with bunch 11 is shown by the modeling to be characteristic of a dominant contribution from the dipole regions of the ring. Also noteworthy is the much greater tune shifts per bunch current at 2.1 GeV relative to those at 5 GeV, significantly greater than can be accounted for by the beam stiffness alone.

III. SIMULATION METHOD

The modeling of electron cloud effects on beam dynamics proceeds in four steps: 1) 3D calculation of the pattern of absorbed synchrotron radiation around the ring including the effects of photon reflections [6], 2) simulation of the interactions of absorbed photons with the vacuum chamber wall which result in the emission of electrons [7, 14, 15], 3) a time-sliced weak-strong model [16, 17] for electron cloud development along a train of positron bunches, including a detailed model for secondary electron emission yield (SEY) from the beampipe walls, and 4) calculations of betatron tune shifts using the space-charge electric field gradient values derived from the cloud buildup model [2, 11, 18, 19]. The secondary electron emission dependencies were parameterized as described in Ref. [20] and the parameters fitted to the tune shift measurements using an iterative optimization procedure. These four steps are described in Sects. III A-III D below.

A. Synchrotron radiation photon tracking

An essential tool in this study is the photon-tracking code Synrad3D [6]. It provides for the generation of individual photons radiated by the positron beam, and incorporates a user-defined 3D model of the vacuum chamber to model the reflection and absorption of photons using the Bmad library [21] and X-ray data from an LBNL database [22]. Figure 4 shows a plan view of photon trajectories in a region of the CESR ring which includes X-ray beamline exit windows at which incident photons are not included in the tally of photons absorbed in the vacuum chamber walls.

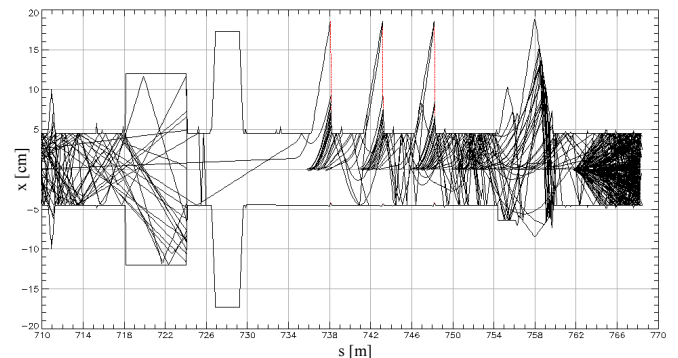


FIG. 4. Modeled photon trajectories in a section of the CESR ring which includes various vacuum system components as well as X-ray beam exit ports. Projections of the horizontal position x of the photons relative to the positron reference orbit are shown. The positrons travel in the direction of increasing s coordinate. The red vertical lines represent the exit port windows; any photon hitting those surfaces are terminated and excluded from the absorbed photon rate.

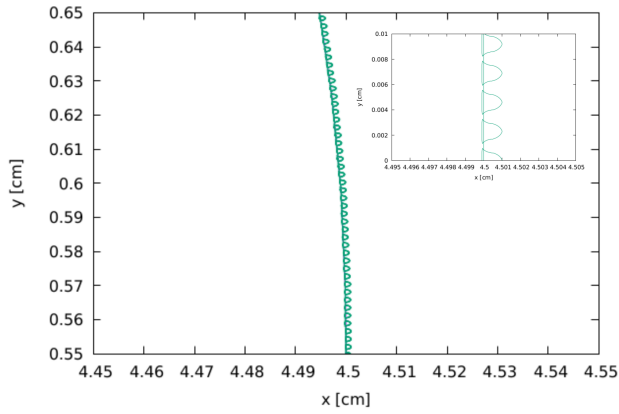


FIG. 5. Schematic diagram of the 10- μ m-deep grooves on the CESR vacuum chamber wall used in the photon reflectivity model.

Photon reflectivity plays a crucial role in electron cloud buildup, since it determines the distribution of photon absorption sites around the ring. Absent photon reflectivity, few photons could be absorbed on the top and bottom of the beampipe, where photoelectron production is the primary source of cloud generation in the vertical plane containing the beam.

A micro-groove structure on the surface of the vacuum chamber has been measured using atomic force microscopy and studied in X-ray beams [23]. These grooves are roughly parallel to the beam axis and are understood to be caused by the beampipe extrusion process. Their effect is taken into account separately from the 100-nm RMS surface roughness parameter used in the diffuse scattering in Synrad3D by incorporating the groove structure into the beampipe model. Figure 5 shows a diagram of the modeled grooves used in the photon-tracking simulation, and Fig. 6 shows the effect of the grooves on the photon tracks.

The transverse absorption location distribution in Fig. 7 shows the consequence of the larger reflection angles from grooves. The absorbed photon rate on the top and bottom of the beampipe increases by a factor of about three.

The reflectivity is also critically dependent on the material composition of the vacuum chamber wall. Figure 8 shows the fraction of photons reflected as a function of photon energy for a 5° grazing angle for aluminum with and without C and CO surface layers. The data were obtained from the LBNL database [22]. In validating our modeling studies, we have chosen to use the 5-nm CO layer, as motivated in Ref. [23].

The photon tracking simulation identifies 10^6 locations around the CESR ring where photons are absorbed, along with the energy and incident angle of the photon. Figure 9 a) shows the linear density per beam particle of absorption sites around the 768-m-circumference CESR ring. The higher densities near the former collider interaction regions at $s=0$ and $s=384$ m result from the

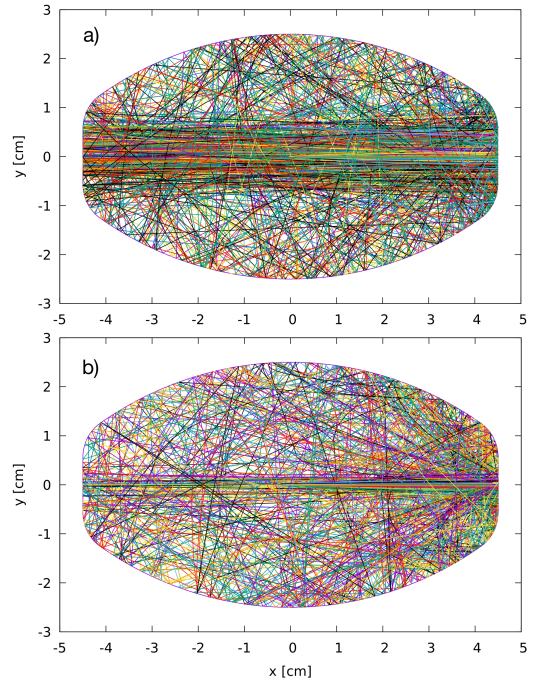


FIG. 6. Examples of photon trajectories a) without the groove pattern on the vacuum chamber wall, and b) with grooves. The groove pattern results in significantly enhanced scattering out of the horizontal mid-plane. The apparent curvature in the tracks is a consequence of the longitudinal bend in the reference trajectory in the dipole.

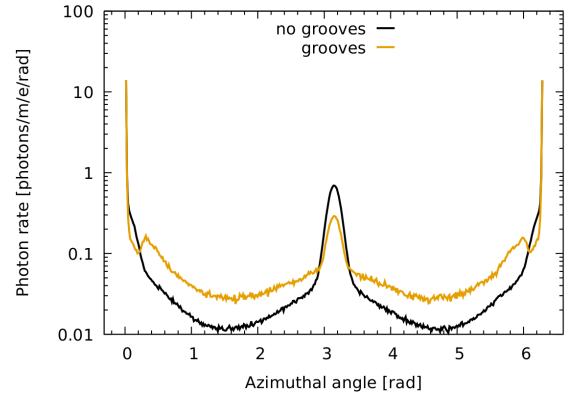


FIG. 7. Comparison of the azimuthal absorption location of the absorbed photons when the micro-grooves are introduced in the CESR vacuum chamber geometry. The azimuthal angle is defined to be 180° in the horizontal plane containing the beam axis on the inside of the ring.

higher-strength dipole magnets which provide for the straight sections where detectors were formerly installed. The energy distribution of the absorbed photons is shown in Fig. 9 b) up to an energy of 500 eV. About half of the absorbed photons carry an energy below this limit. The critical energy of the synchrotron radiation is 3.7 keV in the main arcs and can reach 10.4 keV near the former interaction regions. The distribution in the number

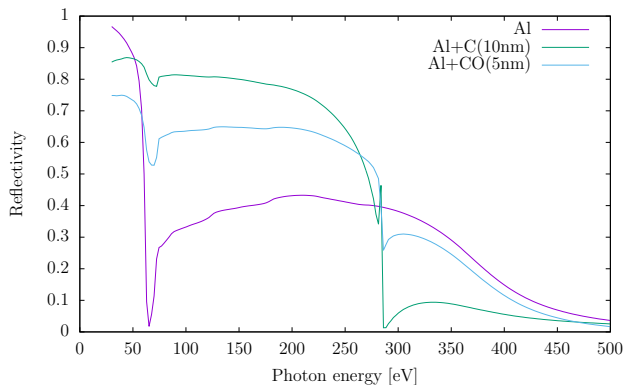


FIG. 8. Smooth-surface photon reflectivity versus photon energy for aluminum, aluminum with a 10-nm carbon layer, and aluminum with a 5-nm carbon monoxide layer, for photons incident at a 5° grazing angle.

of reflections prior to absorption is shown in Fig. 9 c). About half of the absorbed photons were absorbed on the first wall strike. The photon energy is conserved in the modeled reflection process. However, since the reflection probability is a strong function of the incident photon energy, the photons absorbed after undergoing a prior reflection are generally of much lower energy.

Only reflected photons strike the top, bottom and inner walls of the vacuum chamber. The typical number of reflections before absorption depends on the transverse azimuthal angle Φ_{180} of the absorption site location, where Φ_{180} ranges from -180° to $+180^\circ$ with its origin in the mid-plane on the outside of the ring. Figure 10 a) shows the dependence on this angle of the average number of reflections prior to absorption. Figure 10 b) shows the average number of prior reflections of the photons absorbed on the outer wall of the chamber. Figures 10 c), d) and e) show the distributions in the number of prior reflections for the azimuthal ranges $|\Phi_{180}| < 1.5^\circ$, $1.5^\circ < |\Phi_{180}| < 165^\circ$, and $|\Phi_{180}| > 165^\circ$, respectively. For $|\Phi_{180}| < 1.5^\circ$, 83% of the photons were not reflected prior to absorption.

Due to the correlation of azimuthal angle with number of reflections, and the energy dependence of the photon reflectivity, one expects a correlation of photon energy with azimuthal angle. The dependence of absorbed photon energy on azimuth is shown in detail in Fig. 11. Since the probability for electron emission depends on photon energy, we find that the effective quantum efficiency can depend strongly on azimuthal angle. Figures 11 d), e), and f) illustrate the reason for choosing three distinct azimuthal regions when providing electron production energy distributions to the electron cloud buildup simulation. The average energy of the absorbed photons in the azimuthal ranges $|\Phi_{180}| < 1.5^\circ$, $1.5^\circ < |\Phi_{180}| < 165^\circ$ and $|\Phi_{180}| > 165^\circ$ is 2987 eV, 195 eV and 343 eV, respectively, averaged over the full ring.

We will see below in the section on the Geant4 simulations that the photoelectron production energy depends

strongly on the angle of incidence of the photon on the chamber wall. Figures 12 and 13 show details of the photon angle distributions as functions of azimuthal impact location, summed over the field-free and dipole regions of the ring, respectively. The distributions in photon angle of incidence on the vacuum chamber wall are very different for the field-free and dipole regions, with dramatic consequences for the average quantum efficiency. Generally the photons absorbed in the field-free regions have been multiply reflected and are of lower energy, which enhances the quantum efficiency. However, details of the vacuum chambers, such as gate valves, sliding joints and exit windows result in a complicated pattern of photon incident angles around the ring.

The photon tracking simulation thus provides the longitudinal and transverse location, and incident angle and energy on a photon-by-photon basis. Figure 14 shows the absorbed photon rate in units of photons/m/e⁺/radian as a function of transverse azimuthal absorption location, averaged separately over the a) field-free and b) dipole regions of the ring. The cases of a vacuum chamber material consisting of aluminum, aluminum with a 10-nm carbon layer, or aluminum with a 5-nm carbon-monoxide layer are compared.

B. Geant4-based electron production

Significant progress in simulating low-energy electromagnetic processes has been achieved over the past decade in the Geant4 simulation toolkit [7, 14], including both photoeffect and atomic de-excitation processes in a wide variety of materials.

1. Quantum efficiency

In order to determine the azimuthal dependence of the quantum efficiency, we subdivide the vacuum chamber wall into 720 azimuthal bins. The grazing angle and energy distributions of photons absorbed in each bin is determined by the photon tracking code. Given a sample of photon energies and angles of incidence, the Geant4 code is used to generate 10^5 photoabsorption events, determining the rate of emitted electrons summed over the bin. Examples of such events are shown in Fig. 15.

We thus obtain a value for the electron production rate specific to the photon incident angle and energy distribution in each azimuthal bin, including (relatively rare) multi-electron production events. Figure 16 shows the detail with which Geant4 calculates average electron production rates for various wall materials.

The dependence of the quantum efficiency on the incident angle of the absorbed photon is very strong in the Geant4 modeling, as illustrated in Fig. 17, favoring more grazing angles. We recall that the average incident angle of the absorbed photons in the azimuthal ranges $|\Phi_{180}| < 1.5^\circ$, $1.5^\circ < |\Phi_{180}| < 165^\circ$ and $|\Phi_{180}| > 165^\circ$ is

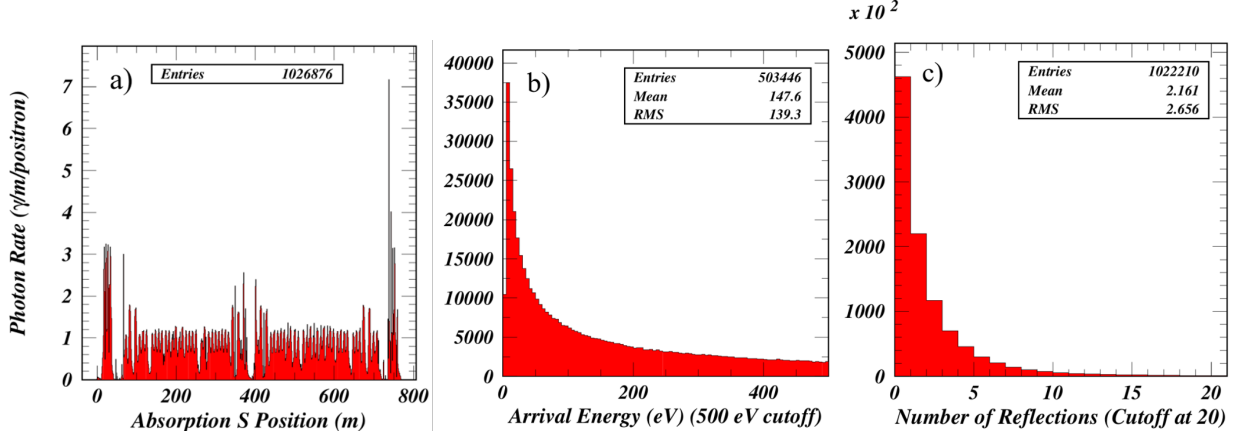


FIG. 9. Distributions of absorbed photons in a) absorption location along the CESR ring, b) photon energy and c) number of prior reflections.

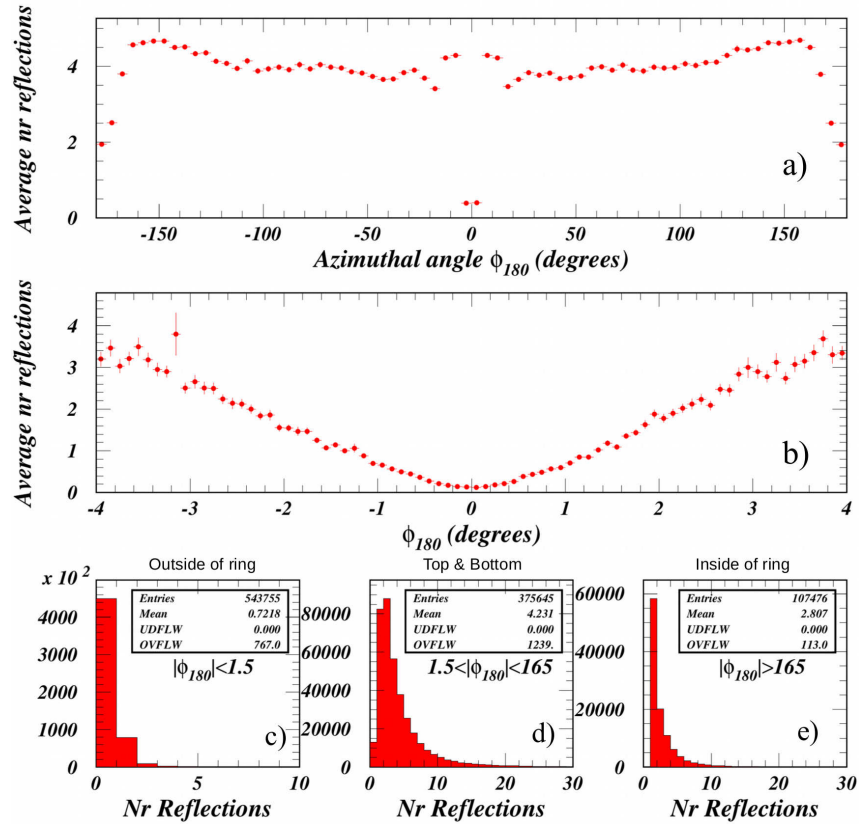


FIG. 10. Average number of prior reflections for absorbed photons summed over the full ring a) as a function of the azimuthal location on the vacuum chamber wall, Φ_{180} , and b) in the narrow range $|\Phi_{180}| < 4^\circ$. The distribution in the number of reflections are shown for the three azimuthal regions c) $|\Phi_{180}| < 1.5^\circ$, d) $1.5 < |\Phi_{180}| < 165^\circ$, and e) $|\Phi_{180}| > 165^\circ$.

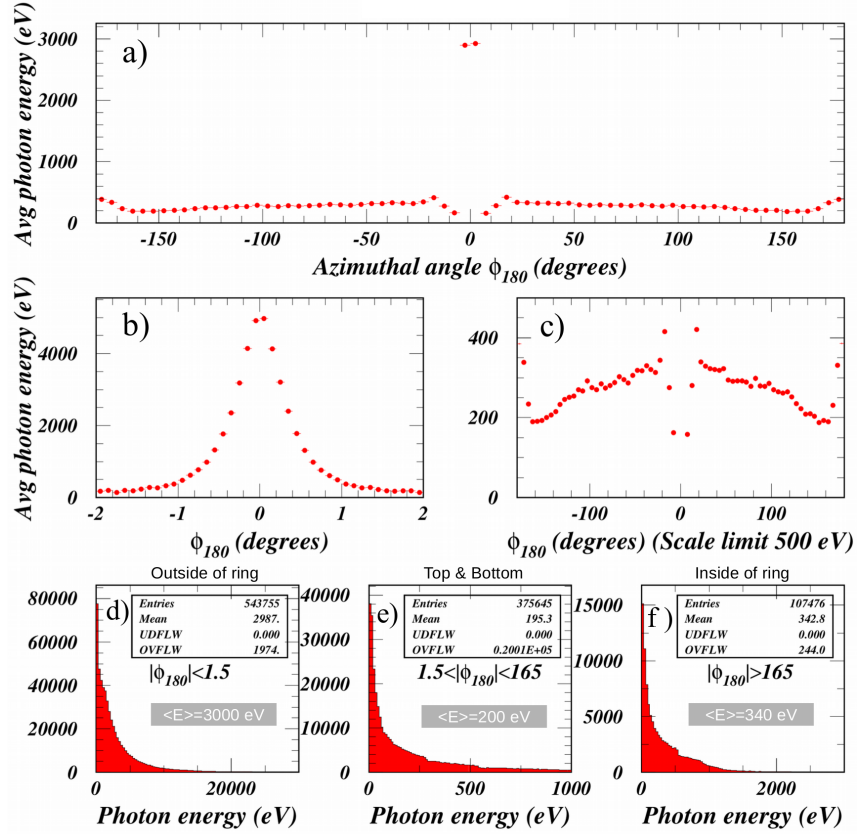


FIG. 11. Average energy of the absorbed photons summed over the full ring a) as a function of the azimuthal location on the vacuum chamber wall, Φ_{180} , b) in the narrow range $|\Phi_{180}| < 2^\circ$, a region rich in unreflected photons, and c) the full azimuthal range, but with the vertical scale limited to a maximum of 500 eV to show details of the energy distribution for multiply reflected photons. The photon energy distributions are also shown for the three azimuthal regions for which electron energy distributions were provided to the electron cloud buildup simulation: d) $|\Phi_{180}| < 1.5^\circ$, e) $1.5 < |\Phi_{180}| < 165^\circ$, and f) $|\Phi_{180}| > 165^\circ$.

20.14°, 9.66°, and 13.05° (2.27°, 5.77°, and 5.55°), in the field-free (dipole) regions, respectively.

Figure 18 shows azimuthal distributions in average quantum efficiency obtained from the Geant4 simulations for the 5.3 GeV positron beam. The resulting distributions in electron production rate in the 720 azimuthal bins provided to the electron cloud buildup simulation code for the case of the aluminum chamber with the 5-nm CO layer are shown in Fig. 19. The integrated rates are 0.0454 and 0.0839 electrons/m/positron for the field-free and dipole regions, respectively. Prior to our development work, only these two quantities and two values for effective average reflectivity around the ring served to describe the photoelectron seeding for the EC buildup simulation code [16].

2. Photoelectron energy distributions

In addition to the determination of quantum efficiencies, we obtain energy distributions of the photoelectrons in each of the three azimuthal regions $|\Phi_{180}| < 1.5^\circ$, $1.5 < |\Phi_{180}| < 165^\circ$ and $|\Phi_{180}| > 165^\circ$ by simulating 10^6 events in each region, again using absorbed photons from

the photon tracking code. These distributions are shown for the CESR dipole regions in Fig. 20. Within each of these three angular regions, electron energy distribution is roughly independent of azimuthal angle. The quantum efficiency values and photoelectron energy distributions are obtained separately for the field-free and dipole regions of the ring, resulting in a total of 1.5×10^8 simulated events to provide input to the electron cloud buildup simulations.

The simulation results for the photoelectron energy distributions show substantial high-energy tails, resulting in an average energy in the azimuthal ranges $|\Phi_{180}| < 1.5^\circ$, $1.5 < |\Phi_{180}| < 165^\circ$ and $|\Phi_{180}| > 165^\circ$ of 761 eV, 99 eV and 120 eV (662 eV, 78 eV and 110 eV), for the field-free (dipole) regions, respectively. These three energy distributions, as well as the average electron production rates in 0.5° azimuthal bins are provided separately for the field-free and dipole regions of the CESR ring as input to the electron cloud buildup calculations described in [13]. Our modeling has shown that it is important and, to an accuracy acceptable for comparing to the measurements, sufficient to differentiate between the field-free and dipole-occupied regions, comprising 17% and 66% of the ring, respectively. Control buildup sim-

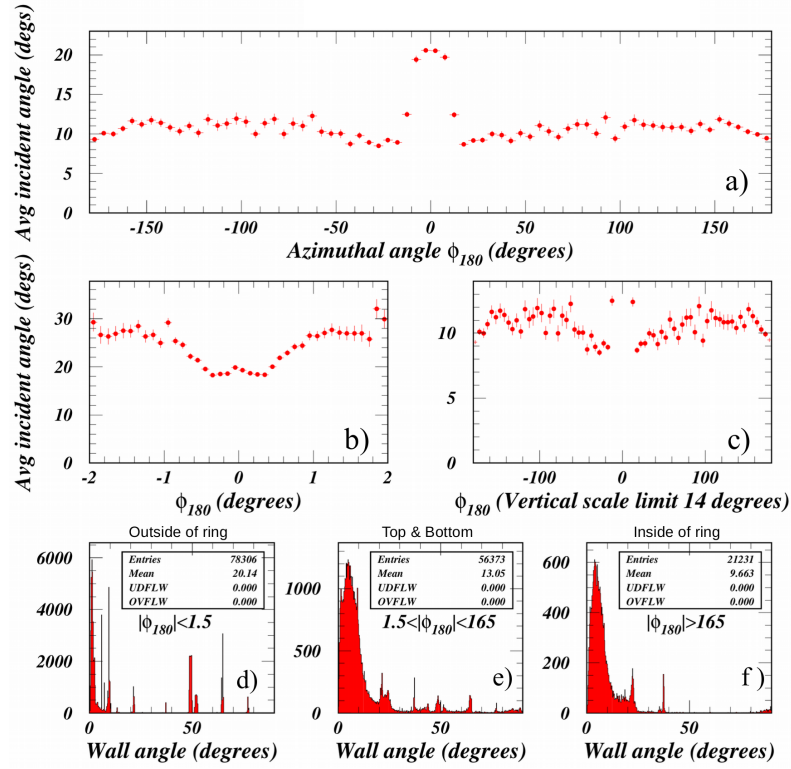


FIG. 12. Average angle of incidence $\langle \theta_{\gamma}^{\text{inc}} \rangle$ of the absorbed photons summed over the field-free regions of the CESR ring a) as a function of the azimuthal location on the vacuum chamber wall, Φ_{180} , b) in the narrow range $\Phi_{180} < 2^\circ$, and c) in the full azimuthal range, but with the vertical scale limited to a maximum of 14° in order to show details of the angular distribution for multiply reflected photons. These distributions are also shown for the three azimuthal regions d) $|\Phi_{180}| < 1.5^\circ$, e) $1.5 < |\Phi_{180}| < 165^\circ$, and f) $|\Phi_{180}| > 165^\circ$.

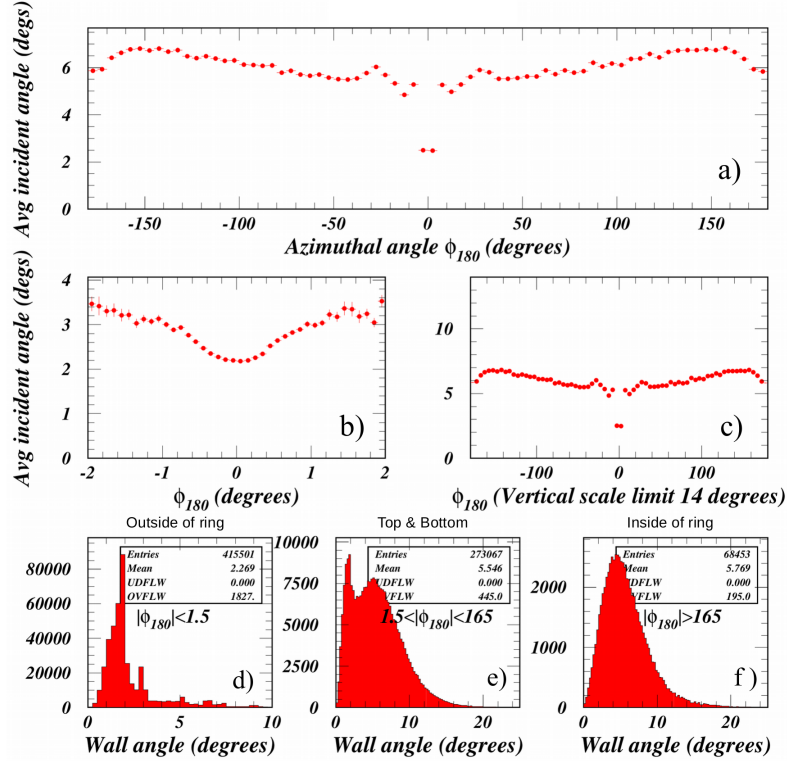


FIG. 13. Average angle of incidence $\langle \theta_{\gamma}^{\text{inc}} \rangle$ of the absorbed photons summed over the dipole regions of the CESR ring. These distributions can be compared to those summed over the field-free regions of the ring shown in Fig. 12. The dependence of quantum efficiency on incident photon angle results in very different photoelectron production rates in the field-free and dipole regions.

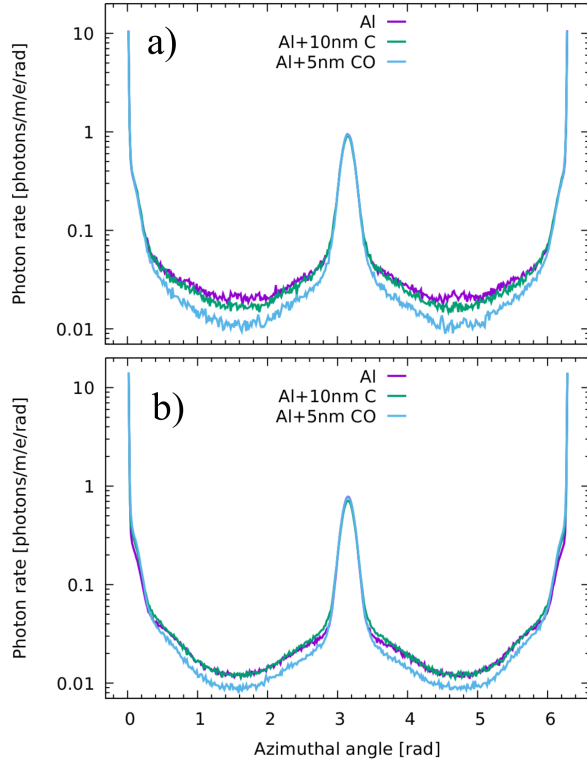


FIG. 14. Azimuthal distribution of photon absorption rate averaged over a) field-free and b) dipole regions of the CESR ring.

ulations in quadrupole and other magnetic field environments show the contribution to the simulated tune shift values from the remaining 17% of the ring to be at the level of a percent.

The electron production energy distribution is of particular importance, since the dependence of, for example, betatron tune shifts varies dramatically, with beam bunch population between 0.6×10^{10} and 9.5×10^{10} positrons/bunch. The associated beam kicks for electrons produced at the wall can be comparable to the electron production energies. These Geant4 simulations show that the primary sources of high-energy electrons (>100 eV) are atomic de-excitation processes, such as the Auger effect. The contribution of such electrons to cloud development is greater at lower bunch population, since their kinetic energies provide for higher subsequent secondary yields, replacing the effect of strong momentum kicks from the beam bunches. Figure 21 shows a schematic diagram of the CESR vacuum chamber illustrating the beam kick quantities in Table II. In an impulse approximation, the beam bunch charge integrated over the bunch passage gives the momentum kick to an electron produced at the wall [25]. An electron generated simultaneously with the passage of the longitudinal center of the bunch, for example, receives half of this kick. We present the kick as the kinetic energy gained by the electron during the bunch passage. The ellipti-

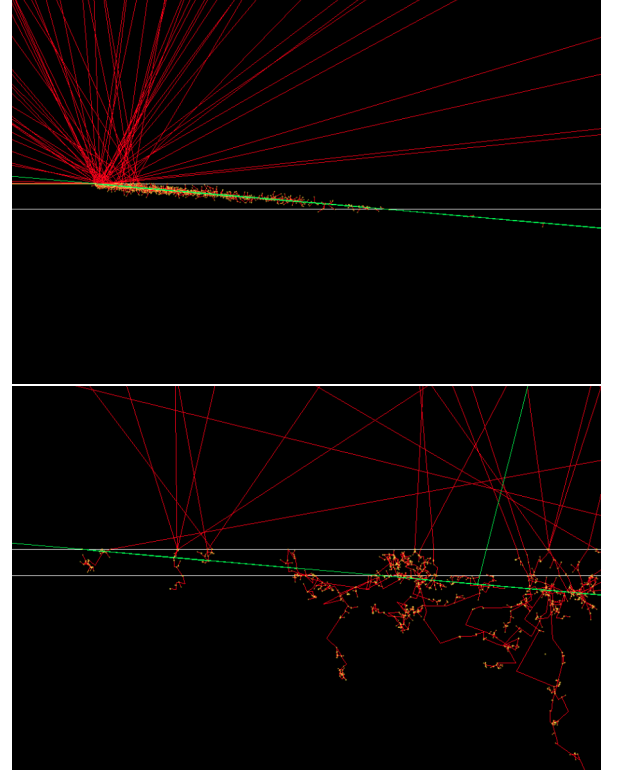


FIG. 15. Tracks from incident photons (green), initially traveling left to right, and subsequently generated electrons (red) in the Geant4 simulation for photon energies of 30 eV (top) and 2 keV (bottom). Low-energy photons interact primarily with the 5-nm CO layer, while the higher energy photons interact in the aluminum. Electrons produced by photoeffect reach the interior of the vacuum chamber via re-scattering, while those produced radially symmetrically by atomic de-excitation processes can exit the wall more directly.

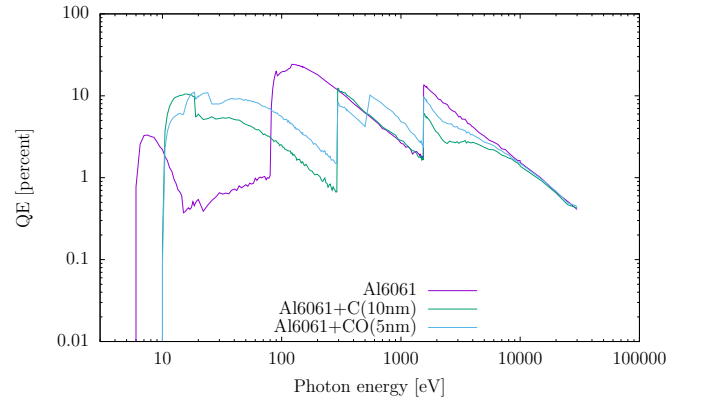


FIG. 16. Quantum efficiency versus photon energy for photons incident at a 5° grazing angle, for the aluminum alloy 6061, aluminum with carbon layer, and aluminum with carbon monoxide layer. The quantum efficiency is sharply enhanced at photon energies above various atomic shell transition energies, such as aluminum L_{II} and L_{III} (73 eV), carbon K (284 eV), oxygen K (543 eV), and aluminum K (1560 eV).

TABLE II. Parameters for the acceleration provided by a positron bunch to a cloud electron located at the vacuum chamber wall on the X or Y axes. These examples correspond to the CESR-TA measurements of betatron tune shifts as well as for the predictions for the 6.0 GeV upgrade of CESR [4, 24]. The total kick values are given as the kinetic energy of the electron following acceleration by the positron bunch in the impulse approximation. The direct and image kick values are signed according to whether they add or subtract from the total kick.

Beam energy (GeV)		2.085		5.289			6.000	
Beam size $\sigma_X \times \sigma_Y \times \sigma_Z$ (mm)		$0.735 \times 0.030 \times 9.2$		$1.44 \times 0.139 \times 15.8$			$1.44 \times 0.139 \times 15.6$	
Bunch population (10^{10})		0.64	1.12	3.25	6.66	9.54	3.52	7.04
Critical radius R_C (mm)		0.73	0.96	2.14	3.1	3.7	2.2	3.2
Maximum kick (keV)		1.2	2.5	3.5	9.0	14.1	3.9	9.8
$X=4.5, Y=0$ cm	Direct kick (eV)	0.16	0.5	41.8	17.6	36	4.9	20.0
	Image kick (eV)	-0.14	-0.44	-41.3	-15.6	-32	-4.3	-17.7
	Total kick (eV)	0.02	0.06	0.5	2.0	4	0.6	2.3
$X=0, Y=2.5$ cm	Direct kick (eV)	0.50	1.6	13.4	56	115	15.8	64.4
	Image kick (eV)	0.60	1.6	13.9	59	120	16.3	66.5
	Total kick (eV)	1.10	3.2	27.3	115	235	32.1	130.9

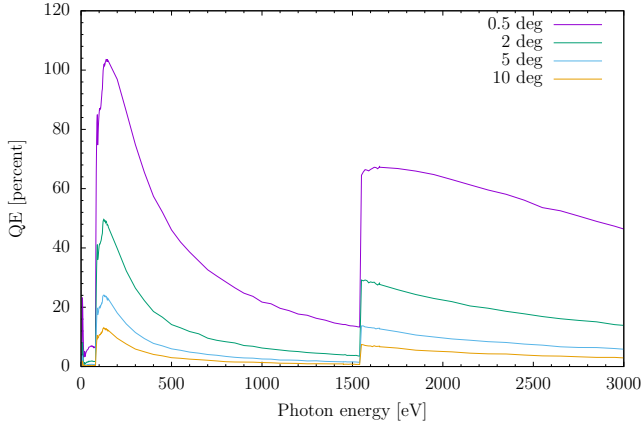


FIG. 17. Quantum efficiency versus photon energy for photons incident at grazing angles between 0.5° and 10° for the aluminum alloy 6061 as modeled in Geant4.

cal shape of the vacuum chamber results in an increased (reduced) kick in the vertical (horizontal) plane from the image charges which ensure the boundary conditions at the wall. The transverse beam size determines the critical radius R_C at which a cloud electron receives the maximum kick during bunch passage. Table II shows these values for the bunch populations and beam sizes for which CESR-TA betatron tune shift measurements are available, and also for the parameters of the upgraded Cornell High Energy Synchrotron Source to be commissioned at 6 GeV in 2019 [10]. The kick corresponding to wall-to-wall traversal of cloud electrons between bunch passages depends on the bunch separation. For 14-ns bunch spacing the kick for horizontal (vertical) wall-to-wall traversal prior to arrival of the succeeding bunch is 36 eV (9 eV). Another relevant consideration in this regard is that SEY is maximum for an electron carrying an energy of about 300 eV.

The wide range of beam kick values causes a great variation in the cloud dynamics as a function of bunch

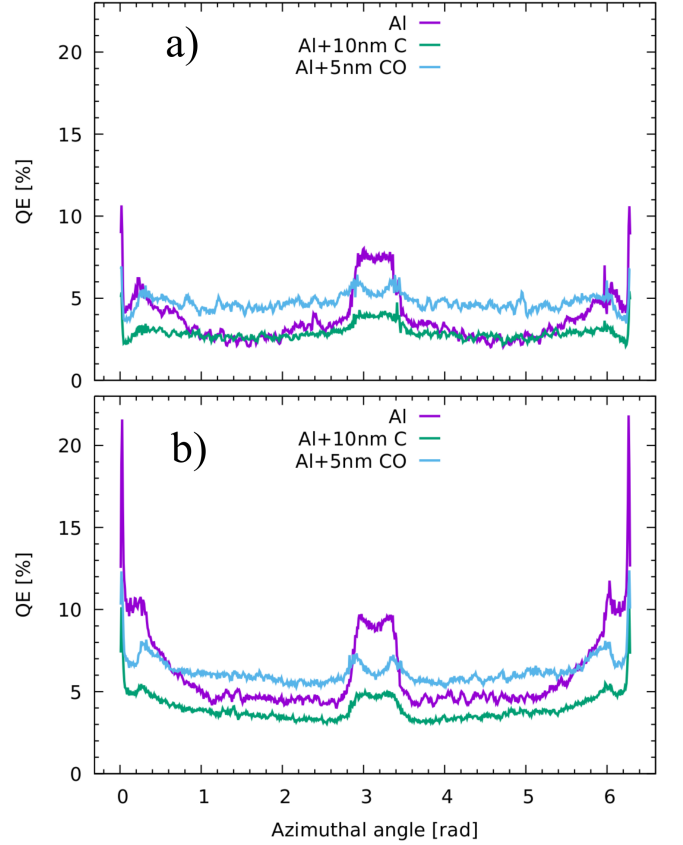


FIG. 18. Azimuthal dependence of quantum efficiency for a) field-free regions and b) dipole regions of the CESR ring for aluminum and aluminum with a carbon or carbon monoxide layer.

population as evidenced in the patterns of observed tune shifts. The interplay between these kicks and the electron production energy distribution is an important aspect of the cloud buildup.

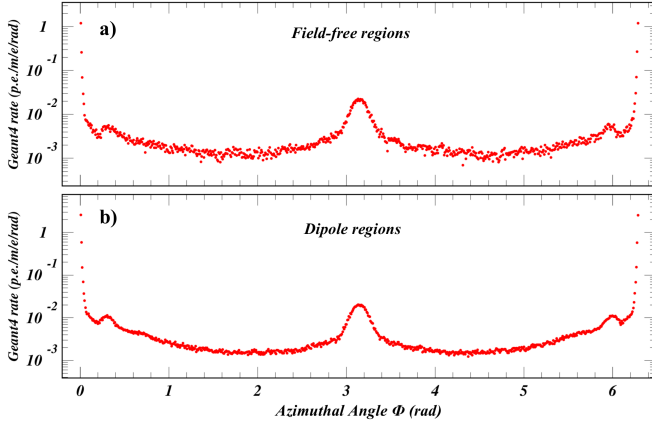


FIG. 19. Electron production rates as a function of azimuthal production location on the vacuum chamber wall for a) field-free regions and b) dipole regions in units of electrons/m/positron/radian.

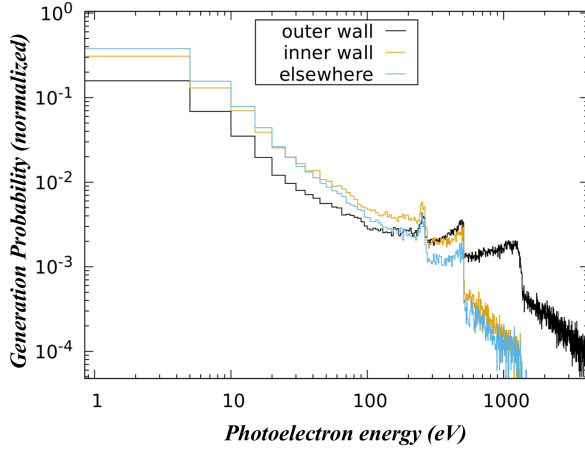


FIG. 20. Electron energy distributions for production locations on the outside wall, inside wall, and elsewhere along the vacuum chamber summed over the dipole regions. Since lower energy photons are more likely to be reflected, the inner wall and elsewhere (including top & bottom) are struck by lower energy photoelectrons than is the outer wall at the mid-plane. These distributions are used as input to the electron cloud build-up simulations.

C. Electron cloud buildup

The EC buildup simulation is based on extensions [11] to the ECLOUD [26] code. The beam size used in these simulations for the 2.1 GeV beam is ring-averaged and weighted by the element lengths for either the 800 Gauss dipole magnets or the field-free regions, and roughly 730 (830) μm horizontally for dipoles (field-free regions) and 20 μm vertically. The large ring-averaged horizontal size is dominated by dispersion. In these simulations we clearly see the pinch effect of the beam attracting the EC (Fig. 22).

Electric field maps on a 15×15 grid of $\pm 5\sigma$ of the transverse beam size are obtained for 11 time slices as the bunch passes through the cloud. The time interval between slices is 20 ps. Figure 23 shows these field

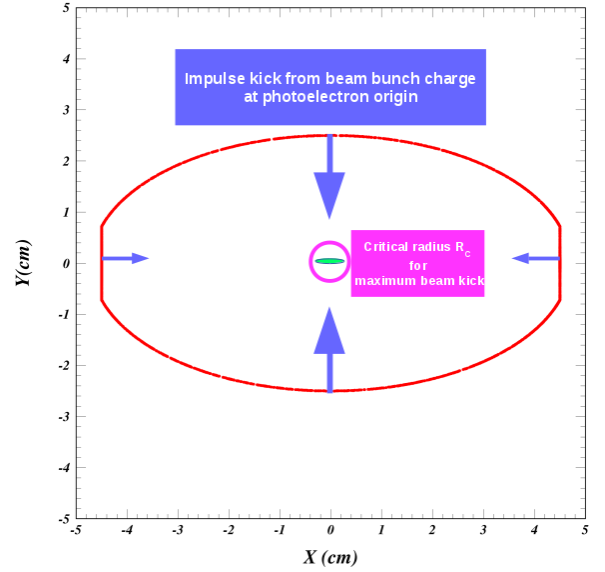


FIG. 21. Schematic diagram of the laterally truncated elliptical CESR vacuum chamber illustrating the beam kicks for an electron produced at the wall and the radius R_c at which an electron receives the maximum kick. Examples of these quantities are given in Table II.

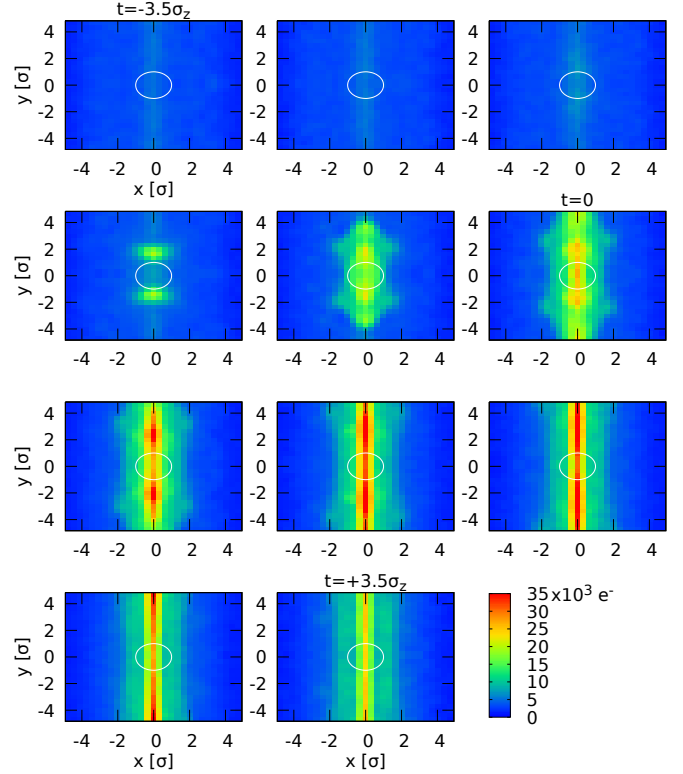


FIG. 22. Transverse charge distributions of the electron cloud in an 800 Gauss dipole field during the passage of the last bunch of the 30 bunch train at 0.7 mA/b at 2.1 GeV, in the central region ($\pm 5\sigma$ of the beam size) for 11 time slices spanning $\pm 3.5\sigma_z$. The RMS beam size is shown as a white circle. Time increases from left to right, top to bottom. The time between slices is 20 ps.

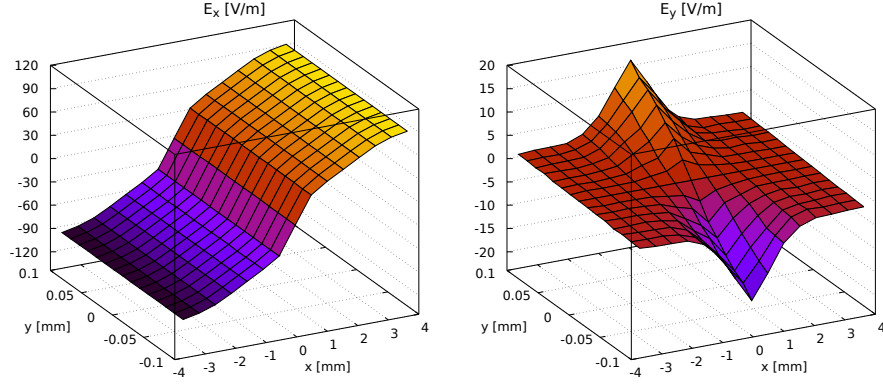


FIG. 23. Space-charge electric field maps in a region of $\pm 5\sigma$ of the transverse beam size for the central time slice of the last bunch of the 30 bunch train at 0.7 mA/b at 2.1 GeV, corresponding to the sixth picture in Fig. 22.

maps in a dipole for bunch number 30 in the 0.7 mA/b train during the central time slice. Since only a small fraction ($\sim 0.1\%$) of photoelectrons are within the $\pm 5\sigma$ region around the beam, it is necessary to combine the results of many ECLOUD simulations to achieve sufficient statistical accuracy in the calculation of the electric field.

The modeled horizontal tune shift values are calculated from the cloud space-charge electric field gradients according to

$$\Delta Q_x = f_{\text{rev}} \frac{e}{4\pi E_{\text{beam}}} \oint \beta_x \left\langle \frac{dE_x}{dx} \right\rangle_{\text{beam}} ds, \quad (1)$$

where f_{rev} is the revolution frequency of 390 kHz, e is the electron charge, E_{beam} is the beam energy, and $\left\langle \frac{dE_x}{dx} \right\rangle_{\text{beam}}$ is the electric field gradient averaged over the transverse charge distribution of the beam. The vertical tune shifts are calculated similarly. The integral over ring circumference is approximated as a sum over the field gradient calculated for each element type weighted by its ring occupancy fraction. The beta function factor is approximated as an average of the beta function over each element type in the ring. Table III shows modeling results and parameter values for each of the tune shift calculations. For the upgraded light source operation at 6 GeV contributions from the newly introduced combined-function (DQ) magnets and the compact undulators (CCU) were included. The CCU magnetic field was modeled as a dipole field, providing an upper limit to the cloud buildup estimate, since the longitudinal magnetic field component suppresses EC buildup.

The pinch effect, whereby the bunch attracts the nearby cloud as it passes, can be clearly seen in Figs. 24 and 25 as a dramatic increase in electric field gradients during the bunch passage. For an offset bunch (the one being excited) in an on-axis train, the pinched cloud is centered on the offset bunch, even in the presence of a dipole field, as shown in Fig. 26. Thus the kick on the offset bunch due to the pinched cloud can be neglected, and does not contribute to the coherent tune shift, as confirmed by the witness bunch betatron tune measurements

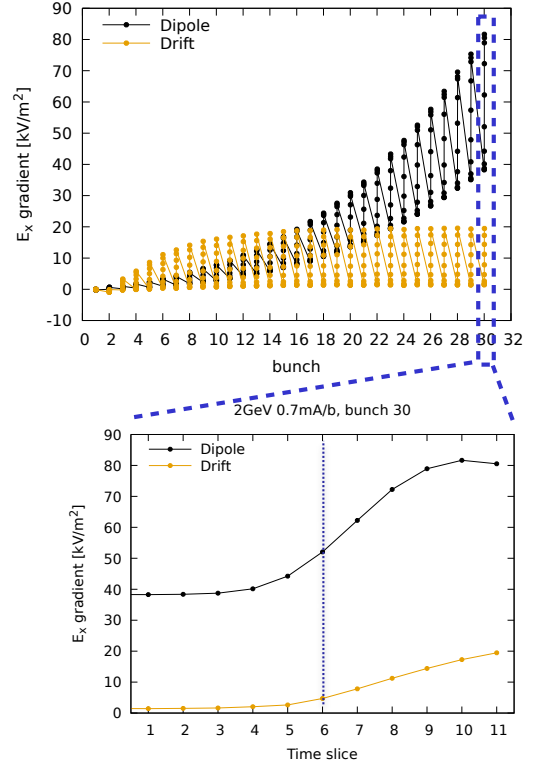


FIG. 24. Top: horizontal electron cloud space-charge electric field gradients for the 11 time slices within each of 30 bunches, for dipoles and field-free regions. Bottom: electric field gradients for the 11 time slices in bunch 30, showing the center of the bunch at time slice 6.

shown in Fig. 27. For this reason, the space-charge electric field gradients immediately prior to the bunch arrival are used when calculating the tune shifts. The pinched cloud does, however, contribute to incoherent tune spread and emittance growth as demonstrated by measurements of beam size in the witness bunch configurations [13].

TABLE III. Modeling results and parameter values used in each of the simulated tune shift calculations. The vacuum chamber shapes used in the EC buildup simulations are approximately elliptical with vertical side walls, except for the undulator chambers, which are rectangular.

Beam energy (GeV)	2.085		5.289		6.000			
	Field-free	Dipole	Field-free	Dipole	Field-free	Dipole	DQ magnet	CCU
Ring fraction (%)	16.3	65.7	16.3	65.7	57.1	23.1	3.7	2.9
Number of photons	1.72×10^5	7.10×10^5	1.56×10^5	7.57×10^5	7.64×10^5	3.26×10^6	3.37×10^5	7.82×10^4
Photon absorption rate ($\gamma/m/e^+$)	0.378	0.370	0.728	0.876	0.833	0.973	1.655	0.3076
Number of electrons	3.65×10^6	4.54×10^6	3.74×10^6	4.55×10^6	3.88×10^6	4.58×10^6	4.65×10^6	4.49×10^6
Electron production rate (p.e./m/e $^+$)	0.02137	0.03144	0.0454	0.0839	0.0603	0.0956	0.1241	0.0317
$\langle\beta_x\rangle$ (m)	16.80	16.50	18.00	17.00	14.10	13.10	1.77	11.07
$\langle\beta_y\rangle$ (m)	24.40	22.90	21.85	21.70	18.10	19.60	15.70	3.49
EC buildup model input parameters								
Vacuum chamber size (H×V) (mm)	90×50		90×50		90×50	90×50	50×22	50×4.5
Dipole field (T)	0	0.0800	0	0.2007	0	0.2277	0.6509	1.0000
Quadrupole field gradient (T/m)	0	0	0	0	0	0	8.762	0

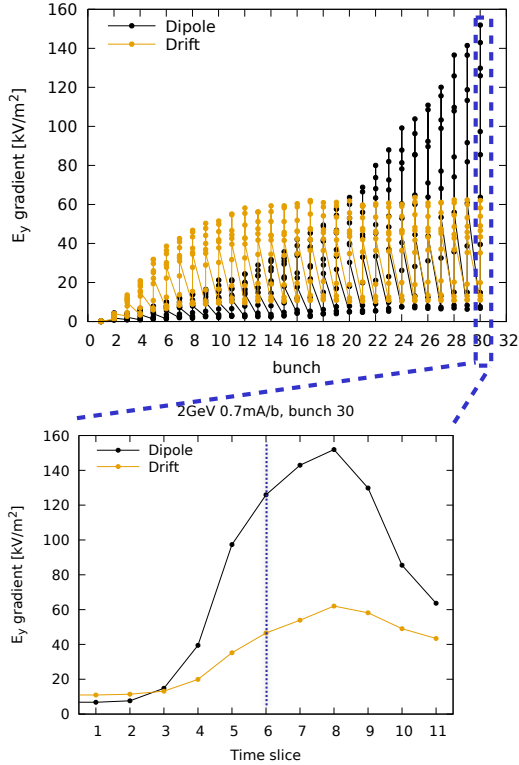


FIG. 25. Top: vertical electron cloud space-charge electric field gradients for the 11 time slices within each of 30 bunches, for dipoles and field-free regions. Bottom: electric field gradients for the 11 time slices in bunch 30, showing the center of the bunch at time slice 6.

D. SEY parameter determination

Secondary electron yield depends on a number of factors such as incident electron energy and angle, chamber wall material and coatings, etc (see list below). Tune shifts from simulation are found to depend strongly on

these details of the secondary yield. The effects of the SEY parameters on the tune shifts can be highly correlated. Direct SEY measurements can provide a good starting point, but it is difficult to accurately measure all of the parameters. Furthermore, the ring-wide averaged SEY may be different than an external measurement of a vacuum chamber sample. To improve agreement between the model and the tune shift measurements, we use an optimizer to fit the model tune shift values to the measurements, varying the SEY parameters. We use the SEY parameters determined for copper in Ref. [20] as a starting point. At each iteration, the EC buildup simulations are run in parallel with the current best SEY parameters, and each parameter increased and decreased by an adaptive increment. The tune shifts from these simulations are obtained, and the Jacobian is calculated and provided to the optimizer. The optimized input parameters are, in the notation of Ref. [20],

- \hat{E}_{ts} : incident electron energy at which the true secondary yield is maximum for perpendicular incidence,
- s : true secondary SEY energy dependence parameter, with $\delta_{ts}(\theta_e, E_0) = \delta_{ts}(\theta_e) s x / (s - 1 + x^s)$, where $x = E_0 / E_{ts}(\theta_e)$, E_0 being the incident electron energy,
- $P_{1,r}(\infty)$: rediffused secondary yield at high incident electron energy,
- $\hat{\delta}_{ts}$: true secondary yield at perpendicular incidence,
- t_1 and t_2 : amplitude of the cosine dependence and power of the cosine in the true secondary yield: $\delta_{ts}(\theta_e) = \hat{\delta}_{ts}[1 + t_1(1 - \cos^{t_2} \theta_e)]$, where $\theta_e = 0$ for perpendicular electron incidence,
- t_3 and t_4 : amplitude of the cosine dependence and power of the cosine in true secondary peak energy: $E_{ts}(\theta_e) = \hat{E}_{ts}[1 + t_3(1 - \cos^{t_4} \theta_e)]$,
- $\hat{P}_{1,e}$: elastic yield in the low-energy limit, and

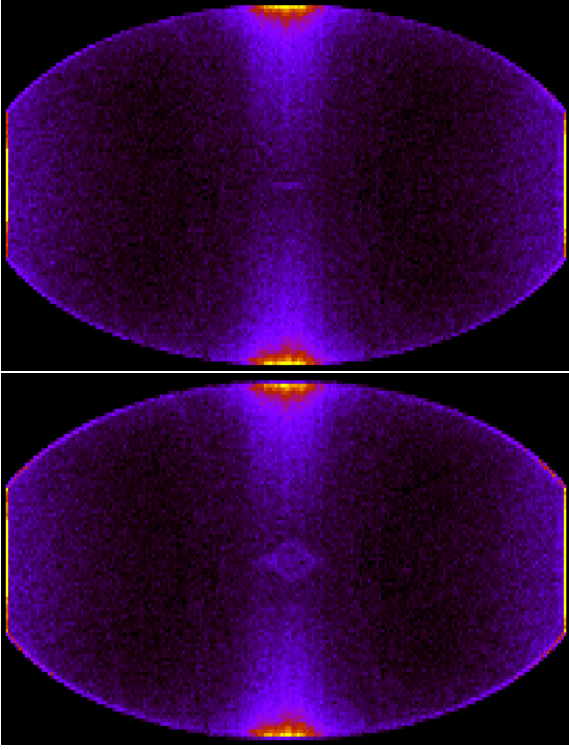


FIG. 26. Simulated electron cloud density during the third (top) and sixth (bottom) of 11 time slices during the passage of bunch 15 (arbitrary), which has been offset from the centered bunch train by 1 mm horizontally to simulate the effect of kicking a single bunch when measuring its tune. The “pinched” cloud is found to be centered on the offset bunch position. The short bunch length (16 mm) bunch hardly modifies the larger built-up cloud. The simulated bunch current is 2 mA/b. At higher currents, the vertical band widens (4 mA/b) and splits into two (6 mA/b).

- ϵ and p : parameters for the energy distribution of the secondaries:

$$\frac{dN}{dE_{\text{sec}}}(E_{\text{sec}}) \propto \begin{cases} \frac{(E_{\text{sec}}/\epsilon)^{p-1} e^{-E_{\text{sec}}/\epsilon}}{\epsilon} & \text{for } E_{\text{sec}} \leq 5\epsilon \\ 0 & \text{for } E_{\text{sec}} > 5\epsilon \end{cases}.$$

The fits are performed simultaneously over all tune shift data at 2.1 and 5.3 GeV shown in Figs. 2 and 3. Table IV compares the optimized parameters to those determined for a copper surface in Ref. [20]. The range and accuracy of the tune shift measurements provides high sensitivity to a number of these parameters. For example, the true secondary yield $\hat{\delta}_{\text{ts}}$ is determined with an accuracy of better than 3%. On the other hand, the sensitivity to the peak energy angular dependence parameters t_3 and t_4 are poorly constrained. The yield value for the rediffused component of the secondary yield is found to be significantly higher than the value obtained in Ref. [20]; however, it must be noted that there is a high degree of anti-correlation with the elastic yield value (see Fig. 28), which is found to be very low.

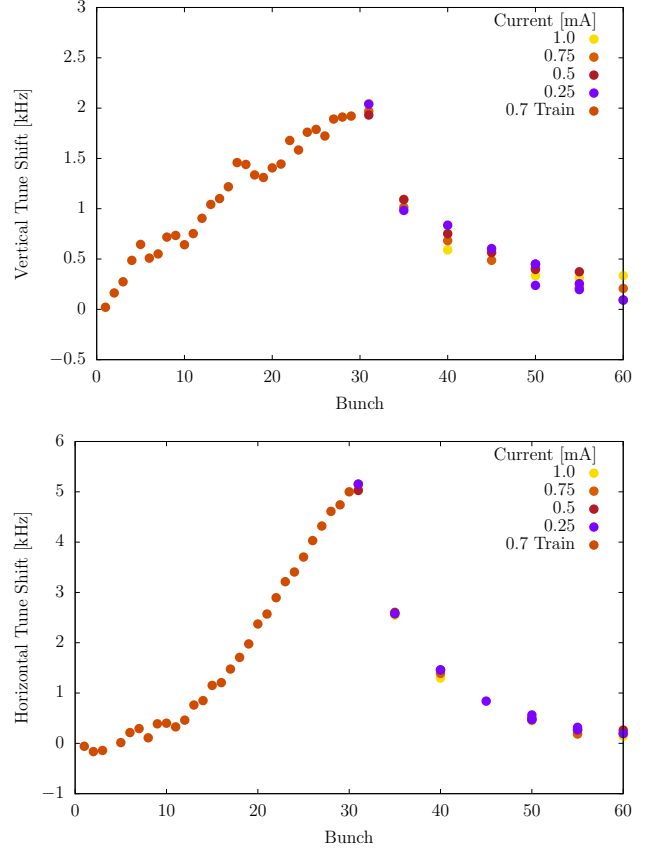


FIG. 27. Vertical (top) and horizontal (bottom) tune shifts measured using the digital tune tracker for a 30 bunch train of positrons at 0.7 mA/b (1.12×10^{10} bunch population) at 2.1 GeV, followed by a witness bunch in bunch positions 31–60 at currents of 0.25, 0.5, 0.75, and 1.0 mA. The vertical tune shift from impedance (~ 1.0 kHz/mA) has been subtracted to show only the contribution from electron cloud. No dependence of the tune of the witness bunch on the witness bunch current is seen, showing that the pinch effect does not contribute to the tune shift.

IV. SIMULATION RESULTS

The comparison of modeled and measured tune shift values is shown in Fig. 29 for the 2.1 GeV positron beam and in Fig. 30 for the 5.3 GeV beam. After optimization of the SEY parameters, agreement at a level better than 10% is found for tune shifts of all bunches in the train. Note that the tune shifts for different locations along the train and for different beam energy and bunch current are in general dependent on distinct phenomena. For example, the horizontal tune shifts increase by about a factor of seven when the bunch current is increased from 0.4 to 0.7 mA/b at 2.1 GeV. The model shows this dramatic effect to be dominated by the dipole sections of the ring. On the other hand, the dipole and field-free regions contribute comparably to the vertical tune shift at 0.4 mA/b and for the first ten bunches of the train at 0.7 mA/b. While the vertical tune shifts saturate at

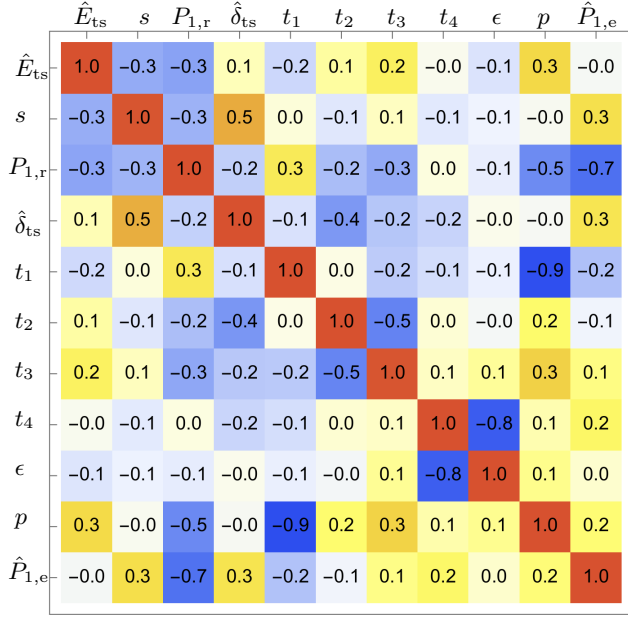


FIG. 28. Correlation matrix for the optimized SEY parameters. Of particular note is that the rediffused yield parameter $P_{1,r}$ is found to be significantly higher than the initial value, while the elastic yield $\hat{P}_{1,e}$ is found to be smaller. However, these two parameters are found to be highly anti-correlated.

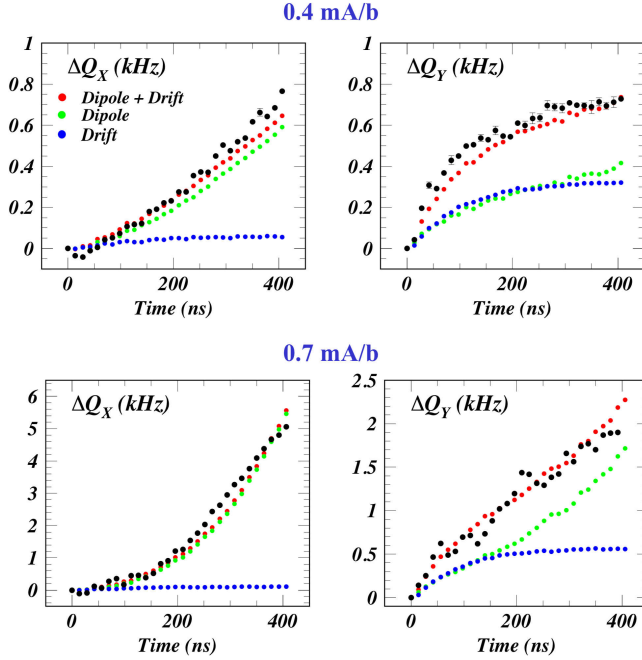


FIG. 29. Comparison of the measured (black points) and modeled tune shift values for the 2.1 GeV 30-bunch train of positrons. Horizontal tune shifts are shown in the left column; vertical tunes shifts are shown on the right. Contributions from the field free regions of the ring are shown in blue; those from the dipole regions are shown in green. The sum of the two contributions is shown in red. The two rows show the results for bunch population values of 0.64×10^{10} and 1.12×10^{10} (0.4 and 0.4 mA/b).

TABLE IV. Initial and optimized secondary emission yield parameters, including the sensitivity to each parameter given in the form of an uncertainty calculated from the Jacobian.

	Initial	Optimized	Uncertainty
\hat{E}_{ts} (eV)	277	260	10
s	1.54	1.58	0.05
$P_{1,r}(\infty)$	0.2	0.39	0.05
$\hat{\delta}_{ts}$	1.88	1.53	0.04
t_1	0.66	0.99	0.2
t_2	0.8	1.5	0.4
t_3	0.70	0.77	0.50
t_4	1.0	1.2	1.0
ϵ (eV)	1.8	3.6	0.4
p	1.0	0.8	0.2
$\hat{P}_{1,e}$	0.5	0.07	0.02

approximately 0.7 kHz for a bunch current of 0.4 mA/b, the dipole regions determine an approximately linear rise during the final 20 bunches at 0.7 mA/b, resulting in a final tune shift value about a factor of three higher. We note that this behavior is accompanied by vertical emittance growth, as described in Ref. [13].

Despite the 5.3 GeV bunch populations exceeding those in the 2.1 GeV measurements by nearly a factor of ten, the vertical tune shifts are less than a factor of two higher than those at 2.1 GeV, a suppression which cannot be accounted for solely by the beam stiffness. The dipole contributions show a threshold behavior at 2 mA/b similar to that observed at 0.7 mA/b for the 2.1 GeV beam. The contribution of the field-free regions saturates at a level of about 0.5–0.8 kHz roughly independently of bunch current at 5.3 GeV, similar to the level calculated by the model at 2.1 GeV for a bunch current of 0.7 mA/b. At the higher bunch currents, the vertical tune shifts begin to show some saturation, which is attributed to the cloud behavior in the dipole regions of the ring. This saturation, or reduction in tune shift increase, is particularly pronounced in the horizontal tune shifts at 5.3 GeV, where again the dominant contributions are from the dipole regions. In fact, the evolution in cloud shape along the train results in increased suppression of the horizontal tune shifts for the higher bunch currents, resulting in a decrease from a level of 3.5 kHz, similar to that measured in the vertical plane, to a value less than 0.5 kHz at 6 mA/b.

This validated model was then employed to predict tune shifts for light source operation at 6 GeV at the design beam current of 200 mA. The new combined-function magnet regions and the compact permanent magnet undulator regions were also included in this study. While their ring occupancy fractions are low (3.7% and 2.9%, respectively), the linear density per positron of absorbed photons can be quite high, owing to the strong magnetic fields and the locations of the magnets in the lattice. Nonetheless, the contributions from these new magnets were found to be small, as shown in Fig. 31.

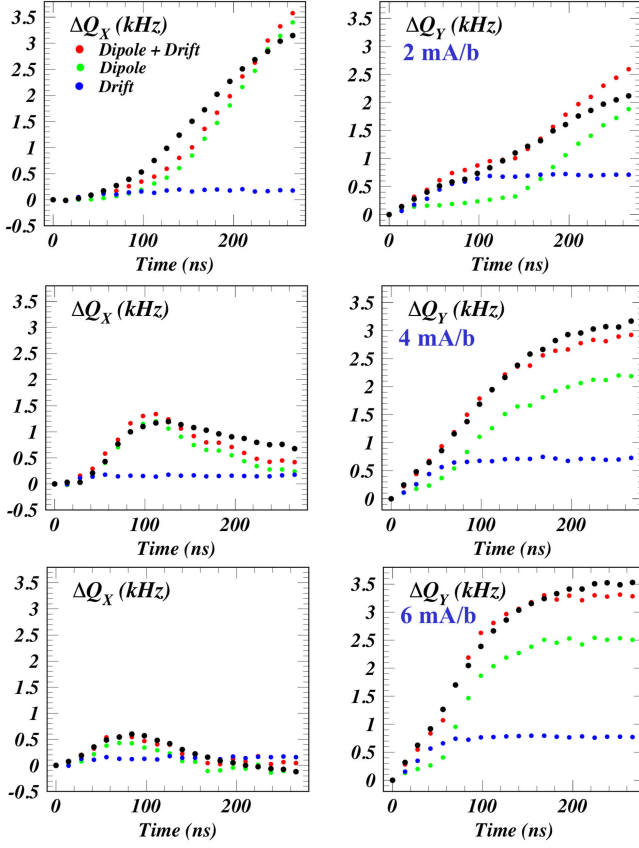


FIG. 30. Comparison of the measured (black points) and modeled tune shift values for the 5.3 GeV 20-bunch train of positrons. Horizontal tune shifts are shown in the left column; vertical tunes shifts are shown on the right. Contributions from the field free regions of the ring are shown in blue; those from the dipole regions are shown in green. The sum of the two contributions is shown in red. The three rows show the results for bunch population values of 3.2×10^{10} , 6.4×10^{10} and 9.6×10^{10} (2.0, 4.0 and 6.0 mA/b).

For the two configurations of 18 equally spaced 5-bunch trains or 9 trains with double the bunch population, the maximum tune shift along the train was found to be less than 2 kHz. While the dipole regions provide the largest contribution to the horizontal tune shifts, the vertical tune shifts show the field-free regions to dominate, owing to the short trains. These results also show that the train-to-train buildup saturates after three trains at most. Since our measurements and modeling of tune shifts in the pre-2019 high-current light source operation indicated that stable operation was maintained with tune shifts of about 3 kHz, we conclude that the tune shifts from electron cloud buildup will not prohibit reliable operation with positrons at the upgraded light source at the design beam current of 200 mA.

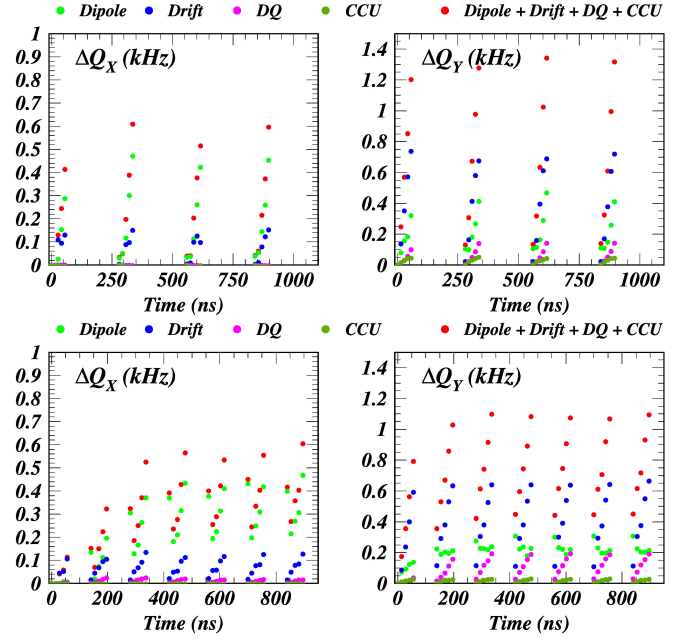


FIG. 31. Modeled horizontal (left) and vertical (right) tune shifts for the 6.0 GeV CESR upgrade. The upper plots show the case of 9 trains of 5 bunches with bunch population 7.0×10^{10} . The lower plots show the case of 18 trains of 5 bunches with bunch population 3.5×10^{10} .

V. SUMMARY

We have obtained improved measurements of betatron tune shifts along trains of positron bunches in the horizontal and vertical planes for a wide range of bunch populations at 2.1 GeV and 5.3 GeV, enabling advances in the predictive power of electron cloud buildup modeling. The Synrad3D and Geant4 simulation codes were employed to eliminate ad hoc assumptions in photoelectron production rates and kinematics endemic to prior buildup simulations. Electron cloud model parameters for secondary electron yield processes were determined through parameterized tune shift modeling optimized to match the measurements. Excellent agreement with the measurements was obtained for a wide variety of tune shift behavior, allowing conclusions relating the tune shifts to various cloud buildup characteristics. The model was employed to predict the magnitude of tune shifts expected during future operation of CESR as a high-brightness 6 GeV positron light source. This study provides a high degree of confidence that stable operation with either 9 or 18 trains of 5 positron bunches at 200 mA beam current can be achieved. The generality and modularity of this modeling procedure successfully addresses the goal of the CESR Test Accelerator program to provide design and diagnostic tools to other present and future accelerator facilities.

VI. ACKNOWLEDGMENTS

The authors wish to acknowledge important contributions from the technical staffs of the Wilson Laboratory. We thank Robert Meller for the design and implemen-

tation of the digital tune tracker for betatron tune measurements. This work is supported by National Science Foundation and by the US Department of Energy under contract numbers PHY-0734867, PHY-1002467 and DE-FC02-08ER41538 and DE-SC0006505.

-
- [1] M. Billing, “The conversion of CESR to operate as the Test Accelerator, CEsrTA. Part 1: overview,” *J. Instrum.* **10**, P07012 (Jul. 2015).
 - [2] “The CESR Test Accelerator Electron Cloud Research Program: Phase I Report,” Tech. Rep. CLNS-12-2084, LEPP, Cornell University, Ithaca, NY (Jan. 2013).
 - [3] S. Poprocki *et al.*, “Incoherent Vertical Emittance Growth from Electron Cloud at CEsrTA,” in *IPAC2016: Proceedings of the 7th International Particle Accelerator Conference, Busan, Korea* (2016), Paper TUPOR021.
 - [4] J. Crittenden *et al.*, “Electron Cloud Simulations for the Low-Emittance Upgrade at the Cornell Electron Storage Ring,” in *NAPAC2016: Proceedings of the North American Particle Accelerator Conference, Chicago, IL* (2016), Paper TUPOB23.
 - [5] S. Poprocki *et al.*, “Incoherent Vertical Emittance Growth from Electron Cloud at CEsrTA,” in *NAPAC2016: Proceedings of the North American Particle Accelerator Conference, Chicago, IL* (2016), Paper WEA2CO03.
 - [6] G. Dugan & D. Sagan, “Simulating synchrotron radiation in accelerators including diffuse and specular reflections,” *Phys. Rev. Accel. Beams* **20**, 020708 (Feb. 2017).
 - [7] S. Agostinelli *et al.*, “Geant4a simulation toolkit,” *Nuclear Instruments and Methods in Physics Research Section A: Accelerators, Spectrometers, Detectors and Associated Equipment* **506**, p. 250 – 303 (2003).
 - [8] J. Crittenden *et al.*, “Simulations of synchrotron-radiation-induced electron production in the CESR vacuum chamber wall,” in *Proceedings of ECLLOUD 2018: Joint INFN-CERN-EuroCirCol-ARIES-APEC Workshop on Electron-Cloud Effects, La Biodola, Elba, Italy*.
 - [9] S. Buechele, “Modeling of Electron Cloud in CHESS and CHESS-U,” REU Report (Aug. 2017).
 - [10] J. Shanks *et al.*, “Accelerator Design for the CHESS-U Upgrade,” (Oct. 2018), <https://arxiv.org/abs/1810.06557>.
 - [11] J. A. Crittenden *et al.*, “Progress in Studies of Electron-cloud-induced Optics Distortions at CEsrTA,” in *Proceedings of the 2010 International Particle Accelerator Conference, Kyoto, Japan, ACFA* (2010), p. 1976–1978.
 - [12] R. E. Meller & M. A. Palmer, “Digital Tune Tracker for CESR,” in *Proceedings of the 2011 Particle Accelerator Conference, New York, NY, IEEE* (2011), p. 504–506.
 - [13] S. Poprocki *et al.*, “Measurements and simulations of electron-cloud-induced tune shifts and emittance growth at CESR,” in *Proceedings of ECLLOUD 2018: Joint INFN-CERN-EuroCirCol-ARIES-APEC Workshop on Electron-Cloud Effects, La Biodola, Elba, Italy*.
 - [14] J. Allison *et al.*, “Recent developments in Geant4,” *Nuclear Instruments and Methods in Physics Research Section A: Accelerators, Spectrometers, Detectors and Associated Equipment* **835**, p. 186 – 225 (2016).
 - [15] J. Apostolakis *et al.*, “Progress in Geant4 Electromagnetic Physics Modelling and Validation,” *Journal of Physics: Conference Series* **664**, p. 072021 (2015).
 - [16] G. Rumolo & F. Zimmermann, “Practical User Guide for ECloud,” Tech. Rep. CERN-SL-Note-2002-016-AP, CERN, Geneva, Switzerland (May 2002).
 - [17] J. A. Crittenden & J. P. Sikora, “Electron Cloud Buildup Characterization Using Shielded Pickup Measurements and Custom Modeling Code at CEsrTA,” in *Proceedings of ECLLOUD 2012: Joint INFN-CERN-EuCARD-AccNet Workshop on Electron-Cloud Effects, La Biodola, Elba, Italy*, R. Cimino, G. Rumolo & F. Zimmermann, Eds., CERN, Geneva, Switzerland (2013), CERN-2013-002, p. 241–250.
 - [18] D. L. Kreinick *et al.*, “Application of Coherent Tune Shift Measurements to the Characterization of Electron Cloud Growth,” in *Proceedings of the 2011 Particle Accelerator Conference, New York, NY, IEEE* (2011), p. 1680–1682.
 - [19] D. L. Kreinick *et al.*, “Using Coherent Tune Shifts to Evaluate Electron Cloud Effects on Beam Dynamics at CEsrTA,” in *Proceedings of ECLLOUD 2010: 49th ICFA Advanced Beam Dynamics Workshop on Electron Cloud Physics, Ithaca, NY*, K. Smolenski, Ed., Cornell University, Ithaca, NY (2013), p. 130–133.
 - [20] M. A. Furman & M. T. F. Pivi, “Probabilistic Model for the Simulation of Secondary Electron Emission,” *Phys. Rev. ST Accel. Beams* **5**, 124404 (Dec. 2002).
 - [21] D. Sagan, “Bmad: A Relativistic Charged Particle Simulation Library,” *Nucl. Instrum. Methods Phys. Res.* **A558**, p. 356–359 (Mar. 2006).
 - [22] B. L. Henke, E. M. Gullikson & J. C. Davis, “X-Ray Interactions: Photoabsorption, Scattering, Transmission, and Reflection at $E = 50\text{--}30,000$ eV, $Z = 1\text{--}92$,” *At. Data Nucl. Data Tables* **54**, p. 181–342 (Jul. 1993).
 - [23] G. F. Dugan *et al.*, “Measurements of X-Ray Scattering from Accelerator Vacuum Chamber Surfaces, and Comparison with an Analytical Model,” *Phys. Rev. ST Accel. Beams* **18**, 040704 (Apr. 2015).
 - [24] K. Rowan, “Revised Stability Predictions for CHESS-U due to Electron-Cloud-Based Tune Shifts,” REU Report (Aug. 2018).
 - [25] J. S. Berg, “Energy Gain in an Electron Cloud During the Passage of a Bunch,” LHC Project Report 97 (Jul. 1997), <https://cds.cern.ch/record/692004/files/project-note-97.pdf>.
 - [26] F. Zimmermann, G. Rumolo & K. Ohmi, “Electron Cloud Build Up in Machines with Short Bunches,” in *ICFA Beam Dynamics Newsletter*, K. Ohmi & M. Furman, Eds., International Committee on Future Accelerators, No. 33, p. 14–24 (Apr. 2004).